Polarization-Resolved Near-Field Spectroscopy of Localized States in *m*-Plane $In_xGa_{1-x}N/GaN$ Quantum Wells

Ruslan Ivanov,[1,*] Saulius Marcinkevičius,[1] Mounir D. Mensi,[1] Oscar Martinez,[1,2] Leah Y. Kuritzky,[3] Daniel J. Myers,[3] Shuji Nakamura,[3] and James S. Speck[3]

[1]*Department of Applied Physics, KTH Royal Institute of Technology, Electrum 229, 16440 Kista, Sweden*
[2]*GdS Optronlab, Física Materia Condensada, Universidad de Valladolid, 47011 Valladolid, Spain*
[3]*Materials Department, University of California, Santa Barbara, California 93106, USA*

(Received 14 October 2016; revised manuscript received 26 April 2017; published 30 June 2017)

We present a polarization, spectrally, and spatially resolved near-field photoluminescence (PL) measurement technique and apply it to the study of wide *m*-plane $In_xGa_{1-x}N/GaN$ quantum wells grown on on-axis and miscut GaN substrates. It is found that PL originates from localized states; nevertheless, its degree of linear polarization (DLP) is high with little spatial variation. This allows an unambiguous assignment of the localized states to $In_xGa_{1-x}N$ composition-related band potential fluctuations. Spatial PL variations, occurring due to morphology features of the on-axis samples, play a secondary role compared to the variations of the alloy composition. The large PL peak wavelength difference for polarizations parallel and perpendicular to the **c** axis, the weak correlation between the peak PL wavelength and the DLP, and the temperature dependence of the DLP suggest that effective potential variations and the hole mass in the second valence-band level are considerably smaller than that for the first level. DLP maps for the long wavelength PL tails have revealed well-defined regions with a small DLP, which have been attributed to a partial strain relaxation around dislocations.

DOI: 10.1103/PhysRevApplied.7.064033

I. INTRODUCTION

Scanning near-field optical microscopy (SNOM) has proven to be a powerful technique to study band potential fluctuations in ternary nitride epitaxial layers, quantum wells (QWs), and light-emitting devices. By providing information on the spatial variation of photo- or electroluminescence spectra with a subwavelength resolution, the technique has enabled studies of material growth mechanisms [1,2], revealed complex relations between band potential fluctuations and recombination [2–10], and enabled the exploration of carrier redistribution and band-filling effects [11,12]. Properties of localized states have been studied in QWs of nonpolar and semipolar crystallographic orientations, and correlations between the surface morphology and properties of photoluminescence (PL) parameters have been established [7–10]. SNOM has also enabled studies of carrier transport on a 100-nm scale [13]. However, within the large body of SNOM research, a parameter that has been largely overlooked is the polarization of the emitted radiation. Partially, this could be attributed to the fact that the near-field polarization is complex [14]; hence, the polarization of PL collected through a fiber probe in the most common illumination-collection mode cannot be analyzed in terms of the polarization of a plane wave. However, the PL polarization can be analyzed using a different experimental geometry, namely, the illumination mode, in which PL excitation takes place through the probe and detection—in the far field.

The majority of SNOM studies have been performed on *c*-plane wurtzite layers and QWs, which, in general, emit unpolarized light. Nevertheless, even for the *c*-plane (In,Ga)N QWs, polarization measurements are found to be useful. In the sole work analyzing PL polarization using SNOM in III nitrides, information on defects was obtained [15]. Polarization-resolved SNOM should be more informative for studies of light emission from QWs of crystallographic orientations other than the *c* plane, namely, nonpolar and semipolar ones, in which radiation is at least partially polarized [16,17]. The emission polarization is related to the valence-band structure and selection rules that are modified, with respect to polar structures, by an anisotropic strain. The degree of the linear polarization (DLP), a parameter commonly used to define PL polarization, is a function of the crystallographic orientation, the energy separation between two topmost valence-band levels, and their population by holes [17]. Hence, its spatial analysis provides information on fluctuations of the inter-valence-band energy. One should also mention that light polarization, apart from serving as a tool for band-structure studies, is also desirable for device applications, e.g., in light-emitting diodes used for the backlighting of liquid-crystal displays [18] and laser diodes because of a higher gain [19]. Thus, high-resolution studies of the DLP may aid the understanding and development of such devices as well.

*rivanov@kth.se

In ternary nitrides, recombination often takes place from localized states. The exact origin of these states, e.g., random alloy composition fluctuations, cation clustering, local strain relaxation at extended defects, etc., should have an imprint on the emitted light polarization. Consequently, by studying spatial variations of the PL polarization with a high spatial resolution, information on properties of the localized states could be obtained.

In that respect, nonpolar *m*-plane $In_xGa_{1-x}N$ QWs studied in this work are especially interesting. Usually they have a broad emission spectrum with a large contribution from the localized states [8,17,20–23]. Moreover, there have been indications that properties of *m*-plane $In_xGa_{1-x}N$ QW PL depend on the surface morphology [24]. Since SNOM enables measurements of the spatial variations of light emission and the morphology simultaneously, maps of PL parameters and their correlation with the morphology features could explicitly reveal relations between growth and the origin of the localized states.

The proposed polarization-resolved SNOM technique could also be applied in other areas than just nitride QWs of nonpolar and semipolar orientations. Measurements of optical polarization with a high spatial resolution could provide valuable information on any light-emitting object with luminescence polarization varying on the subwavelength scale. Among such semiconductor nanowires, quantum dots and quantum dashes, polymer nanofibers, and chiral structures, semiconducting polymer nanostructures and devices, two-dimensional materials, etc., should be noted.

II. EXPERIMENT

Near-field PL measurements are performed at room temperature with a near-field microscope set to operate in the illumination mode. PL is excited through an Al-coated multimode UV fiber probe with a 100-nm aperture diameter. For excitation, 150 fs, 400-nm second-harmonic pulses from a Ti:sapphire laser are used. To maintain the emitted light polarization, PL is collected in the far field with a microscope objective located on the substrate side of the sample, passed through a polarization analyzer and registered by a spectrometer equipped with a liquid-N_2-cooled charge coupled device detector. A typical scan area is 10×10 μm^2 and a scan step is 100 nm. At each point of a scan, a time-integrated PL spectrum is measured. Simultaneously with the optical scans, surface morphology maps are recorded. After the completion of a scan for one PL polarization, the analyzer is turned by 90° and the scan is repeated. The analyzer angle is set to be parallel or perpendicular to the sample **c** axis. Small deviations in the scanned area positions are corrected by adjusting the morphology maps for a perfect overlap. DLP maps are calculated from spectrally integrated PL intensity maps. The spatial resolution of SNOM measurements in the illumination mode are limited by the carrier diffusion. For $In_xGa_{1-x}N$ QWs with large band potential fluctuations, the diffusion length is approximately 100 nm [13]. The near-field PL measurement data are complemented by standard time-integrated far-field PL measured with the same excitation and detection equipment in the 4–300 K temperature range.

The studied samples are single $In_xGa_{1-x}N$/GaN QW structures grown by metal-organic chemical vapor deposition on bulk *m*-plane GaN substrates with a low (about 5×10^6 cm^{-2}) dislocation density provided by Mitsubishi Chemical Corporation. The growth consisted of a 1.2-μm Si-doped GaN buffer layer, a 20-nm undoped GaN layer, an 8-nm undoped $In_xGa_{1-x}N$ QW and a 10-nm undoped GaN cap layer. Most of the presented data concern two samples, the first one of which is grown on an on-axis substrate, and the second one on a substrate miscut at 1° toward the $[000\bar{1}]$ direction. Indium content x, estimated by x-ray diffraction on calibration samples grown under identical conditions, is 0.14 for the on-axis and 0.15 for the miscut QWs. Some additional data are obtained for 11% and 17%–18% In QWs with the same sample geometries. To enable polarization-preserved PL collection from the substrate side of the samples, the backsides have been treated by chemical mechanical polishing.

III. RESULTS AND DISCUSSION

A. Far-field PL

Figure 1(a) shows far-field 300-K PL spectra for $\mathbf{E}\perp\mathbf{c}$ and $\mathbf{E}\|\mathbf{c}$ polarizations as well as 4-K spectrum for $\mathbf{E}\perp\mathbf{c}$ polarized PL for the on-axis QW. PL for the $\mathbf{E}\|\mathbf{c}$ polarization is much weaker and its spectrum is shifted toward shorter wavelengths. This is common for *m*-plane $In_xGa_{1-x}N$ QWs and is explained by the selection rules for optical transitions to the first and second valence-band levels (VBL) [inset to Fig. 1(a)] [17]. These transitions are highly linearly polarized, and the low intensity of the $\mathbf{E}\|\mathbf{c}$ spectra stems from the small thermal population of the second VBL. Figure 1(a) also shows the spectral dependence of the DLP, defined as

$$\mathrm{DLP} = \frac{I_\perp - I_\parallel}{I_\perp + I_\parallel}, \tag{1}$$

where $I_\perp$ and $I_\parallel$ are integrated PL intensities for $\mathbf{E}\perp\mathbf{c}$ and $\mathbf{E}\|\mathbf{c}$ polarizations. Figure 1(b) displays temperature dependence of the DLP for the on-axis and miscut QWs.

Already from the far-field data one can notice several peculiar features. The first one is the large temperature shift of the PL peak [Fig. 1(a)]. The shift, approximately 230 meV, is much larger than the shift of the GaN band gap (70 meV [25]). Then, the difference between the 300-K PL peak energies for $\mathbf{E}\|\mathbf{c}$ and $\mathbf{E}\perp\mathbf{c}$ polarizations, 87 meV for the on-axis and 98 meV for the miscut QWs, respectively, is much larger than the calculated energy difference

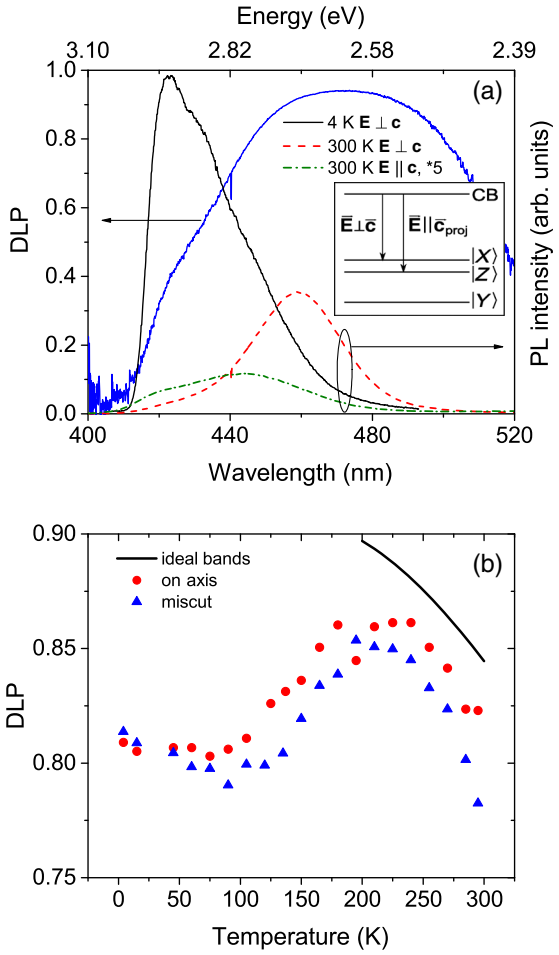

FIG. 1. Spectra of the DLP (blue line) and PL for $\mathbf{E}\perp\mathbf{c}$ (red line) and $\mathbf{E}\|\mathbf{c}$ (green line) polarizations at 300 K, and 4 K $\mathbf{E}\perp\mathbf{c}$ PL spectrum (black line) (a). Temperature dependence of the DLP for the on-axis and miscut QWs (b). The inset to (a) shows schematics of the polarization properties of interband transitions in an m-plane QW.

between the first and the second VBLs of 30 meV [23]. Here, one should note that for wide QWs used in this study quantum confinement effects are small, and the QW level energies are primarily determined by the alloy composition and related strain (Ref. [23] and discussion in Sec. III C). Besides, the DLP temperature dependence is different from the commonly observed decrease determined by the thermal population of the second VBL [9]. It has an S shape, frequently observed for peak wavelengths in polar [26] and sometimes in nonpolar [27] QWs. Finally, while the DLP for the major part of the spectrum is high, it decreases considerably on the short and long wavelength sides. Whereas the DLP decrease at short wavelengths can be explained by the influence of transitions to the second VBL, the decrease in the long wavelength tail signals different properties of the corresponding states. As will be discussed below, all of these observations can be related to the localized states and provide information on their properties.

B. Surface morphology

Maps of the surface morphology for both samples are shown in Fig. 2. Typically, for on-axis m-plane GaN [24,28], the sample surface is formed by overlapping hillocks. The inclination of the hillock planes from the m plane, however, does not exceed 0.5° [28]; thus, an eventual transverse electric field caused by the deviation of the QW plane from the m plane should not affect the QW PL. The hillocks make the surface rough with a root mean square (rms) of about 7 nm. To emphasize the surface undulations, derivatives of the surface morphology at directions perpendicular and parallel to the $\mathbf{c}$ axis (defined as x and y gradients, respectively) are shown in Figs. 2(c) and 2(d). The x-gradient map reveals the major planes of the hillocks; the y gradient distinguishes sub-μm-scale features formed on top of the hillocks. A much smoother surface with rms approximately 2 nm is found for the miscut sample [Fig. 2 (b)]. Here, surface undulations have the form of parallel diagonal striations, which are a manifestation of stable $a+c$ direction steps [28]. The direction of the steps is unrelated to the crystallographic axes.

C. Spatial variations of PL parameters

Figure 3 displays maps of the PL peak wavelength for the $\mathbf{E}\perp\mathbf{c}$ polarization and the DLP for the on-axis and the miscut QWs. In general, near-field spectra of m-plane (In,Ga)N QWs experience large variations in shape, peak wavelength, and full width at half maximum (FWHM) [8]. Average values and standard deviations σ of PL parameters

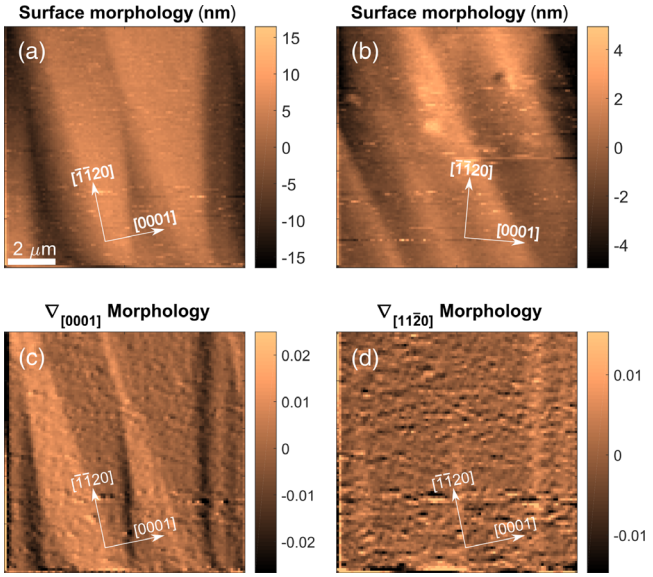

FIG. 2. Surface morphology of the on-axis (a) and miscut (b) QWs. Parts (c) and (d) show morphology gradients for the on-axis sample along the $\mathbf{c}$ and $\mathbf{a}$ axes, respectively.

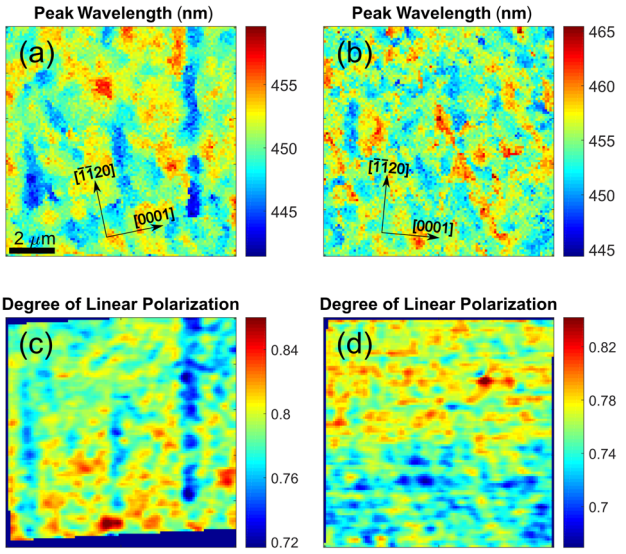

FIG. 3. SNOM maps of the PL peak wavelength (a),(b) for $\mathbf{E}\perp\mathbf{c}$ polarization and the DLP (c),(d) for the on-axis (left column) and miscut (right column) QWs. The dark blue regions on the edges of the DLP maps are caused by the mismatch of the regions scanned for the different analyzer positions.

are gathered in Table I. Some variations can be assigned to the surface morphology (see Sec. III D); however, most of the islands seen in the maps are not morphology related. The presence of well-defined several hundred nanometer-to-micrometer-size islands in the peak wavelength map and the large FWHM show that carriers in the QWs experience a dual localization [29]. The large-scale band potential variations are revealed by the SNOM; the nanometer-scale fluctuations are hidden in the PL linewidth because their dimensions are below the SNOM resolution. For wide QWs, the peak wavelength variations primarily originate from alloy composition fluctuations rather than that of the QW width. This can be demonstrated by energy-level calculations showing that well-width variation of two monolayers, which is a typical fluctuation size [30], would shift the peak wavelength by just 0.6 nm, a much smaller value than the experimentally observed peak wavelength span of approximately 10 nm [Figs. 3(a) and 3(b)]. Assigning the peak wavelength variation solely to the nonuniformity of the alloy composition, islands with shorter and longer peak wavelengths correspond to an average In content variation of about 0.5%. The origin of these islands is not entirely clear; most probably, they are related to the nonuniformity of growth. Nanometer-scale band potential fluctuations can primarily be assigned to random $In_xGa_{1-x}N$ alloy fluctuations [22,31]. As can be seen from the standard deviations of the peak wavelength (reflecting the large-scale band potential variations) and the FWHM (related to the nanoscale fluctuations), the large- and small-scale band potential variations are comparable.

As mentioned above, the $\mathbf{E}\perp\mathbf{c}$ PL peak shift with increasing temperature is much larger than the band-gap shift. This indicates that the peak shift is primarily determined by the carrier redistribution between the localized states and not by the band-gap shrinkage. Increased thermal energy allows a carrier transfer across the potential maxima toward deeper states [12]; the full thermalization, however, is not achieved even at 300 K. This is evidenced by the large FWHM showing that carriers are not gathered at the lowest potential minima, as would be expected for the full thermalization case, but are distributed throughout localization minima of different energies [12,22,23].

In the context of the present study, it is important to note that even though PL is emitted from the deep localized states, its DLP is high. In general, because of the *s*-type symmetry of the conduction band, the DLP is determined by properties of the VBLs. In *m*-plane $In_xGa_{1-x}N$ QWs, the first and second levels originate from the two topmost valence bands [17]. At low temperature, the DLP is determined by selection rules for electron transitions into the first VBL. With increasing temperature, the DLP decreases due to the thermal population of the second VBL. At low carrier densities and high temperatures, this population follows the Boltzmann distribution. For spectrally independent matrix elements for transitions to the first and second VBLs, the DLP dependence on the interlevel energy is expressed by a simple expression:

$$\mathrm{DLP} = \frac{1-\beta e^{-\Delta E/kT}}{1+\beta e^{-\Delta E/kT}}, \tag{2}$$

TABLE I. Statistical parameters of the near-field PL.

Sample	On axis	Miscut
Peak wavelength for $\mathbf{E}\perp\mathbf{c}$, average, σ, nm	450.5 (2.2)	454.9 (2.5)
FWHM for $\mathbf{E}\perp\mathbf{c}$, average, σ, nm	34.8 (2.8)	29.7 (2.3)
FWHM for $\mathbf{E}\perp\mathbf{c}$, average, σ, meV	213 (17)	178 (14)
DLP, average, σ	0.80 (0.02)	0.77 (0.02)
Correlation peak wavelength—DLP	0.21	0.26
Correlation peak wavelength—morphology	0.15	0.09
Correlation peak wavelength—morphology *x* gradient	0.29	−0.13
Correlation peak wavelength—morphology *y* gradient	−0.21	−0.07

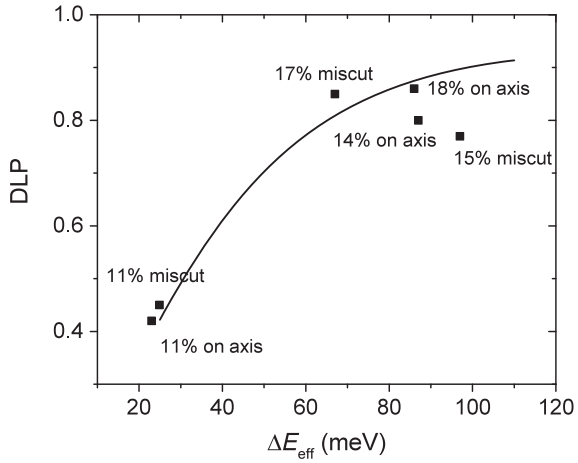

FIG. 4. DLP dependence on the effective energy between first and second VBLs for on-axis and miscut QWs with the In content varying from 0.11 to 0.18. The curve corresponds to Eq. (2) with $\beta = 1$.

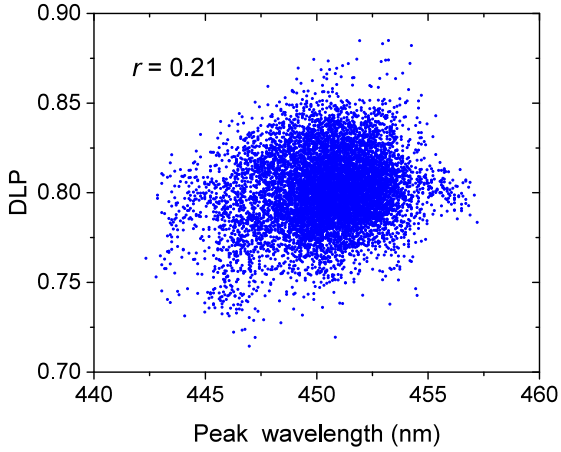

FIG. 5. Correlation between the DLP and the $\mathbf{E}\perp\mathbf{c}$ PL peak wavelength for the on-axis QW.

where k is the Boltzmann constant, T is the lattice temperature, and β is a composite parameter including both the ratio between matrix elements of the considered interband transitions and the ratio between their joint densities of states. The detailed analysis with band parameters taken from Refs. [32,33] shows that $\beta \approx 1$ (see Supplemental Material [34]). This dependence, corrected by 8% for the deviation from the 100% linear polarization for transition into the first VBL, see Sec. III E, is plotted on Fig. 4. The points in the graph correspond to average values of the near-field DLP and the energy difference between 300 K $\mathbf{E}\|\mathbf{c}$ and $\mathbf{E}\perp\mathbf{c}$ PL peak energies. Apart from the analyzed samples, the graph displays values for QWs with a lower and higher In content not discussed in detail in the paper. As one can see, Eq. (2) describes the experimental data quite well. However, even the lowest values in the DLP maps are larger than the ones expected for ideal bands without band potential fluctuations. This observation leads to two important conclusions. First, the *effective* energy separation between the VBLs is larger than the one for the ideal bands. Second, the localized states are formed by the band potential fluctuations caused by alloy composition variations. If the localized states originated from regions of relaxed strain, they would have a much smaller DLP, since relaxation of the compressive strain in *m*-plane QWs leads to a decrease of the valence-band separation and, consequently, an increased population of the second VBL [16,21]. One should note that these conclusions are valid independently of the substrate miscut and the In content, as evidenced by measurements on miscut and on-axis QWs with the In percentage varying from 11% to 18%.

Further information on the valence-band potential variations can be derived from the correlation between the PL peak wavelength ($\mathbf{E}\perp\mathbf{c}$) and the DLP (Fig. 5). As one can see, the correlation is weak with the Pearson product-moment coefficient r equal to 0.21 and 0.26 for the on-axis and miscut samples, respectively. In general, the energy between the first and second VBLs in $In_xGa_{1-x}N/GaN$ QWs should be larger in regions with a lower band gap [27,35,36]. Then, in these areas the second VBL population should be smaller and the DLP larger. Consequently, one would expect a strong correlation between the DLP and the peak wavelength maps. However, this would only happen for similar first- and second-VBL potentials seen by the holes. Since the band potential fluctuations vary on a scale of a few nanometers [22,31], carrier wave functions may cover several potential minima transforming real potentials into *effective* potentials that would depend on the wave-function spread or, in other words, on the effective mass [23]. Carriers with a large effective mass would be confined to a small volume and experience an effective potential close to the real one. On the other hand, carriers with a small mass would spread over several potential minima smoothing the band potential fluctuations and, in effect, experiencing much smaller band potential variations (Fig. 6). Thus, different hole masses in the first and second VBLs could reduce the correlation between the peak wavelength and the DLP.

This situation has been modeled by calculating correlation between the first VBL energy and the interlevel energy for different relative smoothing of the VBLs by the wave-function spread. Considering that the DLP is mainly affected by the population of the VBLs and neglecting conduction band fluctuations [23], this correlation reflects the same physical situation as the correlation between the peak wavelength and the DLP. Here, one should remember that the peak wavelength and the FWHM measured at each pixel of a scan for the $\mathbf{E}\perp\mathbf{c}$ reflect the energy of the first VBL and its inhomogeneous broadening, respectively, averaged over the probe diameter (100 nm). Thus, to simulate the experimental conditions, randomly distributed

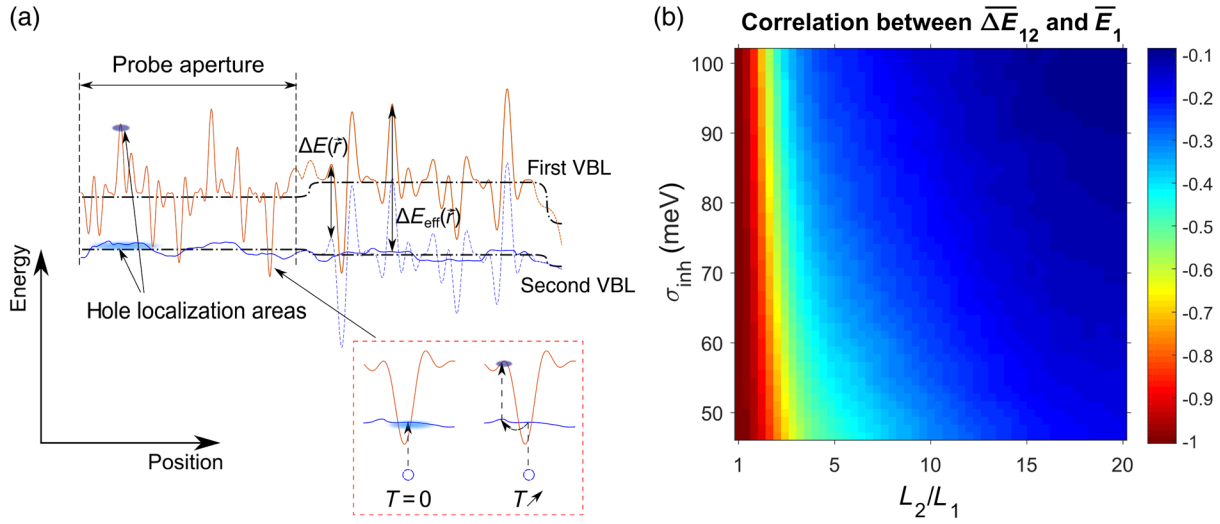

FIG. 6. Real (first and second) and effective (second VBL) potential fluctuations for a small second-level hole effective mass (a). Dash-dotted lines indicate probe-averaged energies of the VBLs. Part (b) shows the calculated correlation between probe-averaged energy of the first VBL ($\overline{E_1}$) and interlevel energy ($\Delta\bar{E}_{12}$) as a function of the hole spread in the second and the first VBLs (L_2/L_1) and inhomogeneous broadening of the first VBL (σ_{inh}).

(3–10)-nm size band potential fluctuations are generated in such a way that the energy average of these fluctuations would match the measured peak energy, and the average of fluctuation amplitude—the average inhomogeneous broadening. The latter quantity is evaluated from the FWHM following Ref. [37]. To estimate the average interlevel energy for a pixel, first the local In content is evaluated from the peak PL wavelength measured at that pixel, and then the interlevel energy is estimated using calculation data of Ref. [23]. Equal fluctuation amplitudes of the potentials of both levels are considered. The effective potential of the first VBL is assumed to be the same as the real one, i.e., no smoothing is applied. For the second VBL, the effective potential is obtained by averaging the real band profile over the distance determined as the wave-function spread in the first level magnified by the ratio of the hole effective masses in the two levels. Spread in the ground VBL is set equal to 5 nm corresponding to the typical distance over which the wave function of holes localized at the first VBL fluctuations decreases by a factor of e. Schematics of the model are illustrated in Fig. 6(a) for the first-to-second VBL effective mass ratio of 8. The simulations are run for each of the ten thousand measurement points, for which the potential fluctuations are generated at random with a constraint that the averages matched the experimental data. The correlation is calculated for different values of the hole spread ratio (L_2/L_1) and the inhomogeneous broadening of the first VBL. The resulting phase diagram is shown in Fig. 6(b).

The diagram shows that the correlation value rapidly decreases with the increased second-level wave-function spread. The experimental peak wavelength-DLP correlation coefficient of 0.21 corresponds to the localization length ratio of 6 to 7, implying the same difference in the hole effective masses. Thus, the very weak correlation between the peak wavelength and the DLP indeed shows that the hole effective masses in the first and second VBL are largely different. The difference of the effective band potential fluctuations for the first and second VBLs affects the effective interlevel energy and the DLP as well.

Another observation pointing toward smaller effective band potential fluctuations in the second VBL is the temperature dependence of the peak DLP [Fig. 1(b)]. Contrary to the expected monotonous decrease caused by the increased thermal population of the second VBL, the DLP exhibits a rise at temperatures between approximately 50 and 200 K. The different effective potentials for the first and second VBLs imply that the second-level energy may become lower than that of the first level at locations with sufficiently large amplitude of the potential fluctuations (> 30 meV), see inset to Fig. 6(a). The nonthermal hole distribution at low temperatures would lead to the occupation of the second-level states that, in the case of similar effective band potentials, would remain empty. Such a behavior would result in a smaller low-temperature DLP. With increased temperature, hole redistribution toward deeper potential minima takes place [12], reducing the population of the second level and increasing the DLP. At high temperatures, the DLP increase changes to a decrease because of an increasing thermal population of the second VBL. This decrease, evaluated for ideal bands with Eq. (2) using the $\mathbf{E}\|\mathbf{c}$ and $\mathbf{E}\perp\mathbf{c}$ PL peak-energy difference (87 meV) as the effective interlevel energy, is shown by a solid line in Fig. 1(b). The calculated values and, especially, the slope, are close to the experimental data.

D. Correlation between optical and morphological features

Now, let us examine the influence of the surface morphology on the near-field PL and the DLP. In m-plane GaN, the morphology depends on the growth conditions and, in particular, on the substrate orientation [24,28]. Substrates cut at a small angle with respect to the **c** axis typically have a smoother surface, which is also evidenced in the current work (Fig. 2). A comparison between large-scale (hundreds of micrometers) mapping of cathodoluminescence and the surface morphology suggests that the emission from different facets of the surface pyramids has different spectra [24]. Here, we exploit the capability of the polarization-resolved SNOM to measure surface morphology and PL simultaneously and examine the correlation between the morphology and the PL properties, including the DLP.

By inspecting the morphology and the optical maps for the on-axis QW sample (Figs. 2 and 3), one can notice a slight correlation between them. The largest correlation with $r = 0.29$ occurs between the peak wavelength and the morphology x gradient, which defines slopes of pyramidal hillocks toward the **c** axis. The correlation is a direct indication that different pyramidal facets have a slightly different average In content. The small morphology features, primarily oriented along the **c** axis and most clearly seen in the y-gradient map, also have some effect on the PL peak wavelength, resulting in $r = -0.21$. This reveals that slight peak wavelength and In content variations occur on the **a**-direction slopes as well. For the miscut sample, the correlation between the morphology and the PL data is negligible. However, standard deviations of the peak wavelength and the DLP differ little for the on-axis and miscut samples. This shows that the nanoscale alloy composition variation largely prevails over the difference of the In uptake at different facets and is the main mechanism for the inhomogeneous broadening and the spatial variation of the emission wavelength. This is an important result for m-plane QW applications showing that the miscut does not play a decisive role in determining the overall emission linewidth and the emitted light polarization.

E. Spectral dependence of PL polarization

The spectral dependence of the far-field DLP [Fig. 1(a)] suggests that states emitting at the short and long wavelength slopes of the PL peak have different properties from the states emitting in the peak center. To get a deeper insight into this effect and study its spatial variation, the near-field PL spectra are deconvoluted into three (four for $\mathbf{E}\|\mathbf{c}$) Gaussian peaks [Figs. 7(a) and 7(b)], the parameters of which are plotted as separate maps. Constraints applied in the deconvolution are the following: (i) peak wavelengths and linewidths for the constituent peaks are the same for $\mathbf{E}\perp\mathbf{c}$ and $\mathbf{E}\|\mathbf{c}$ spectra measured at a particular point of a scan; (ii) the peak wavelength of an $\mathbf{E}\perp\mathbf{c}$ spectrum is set as

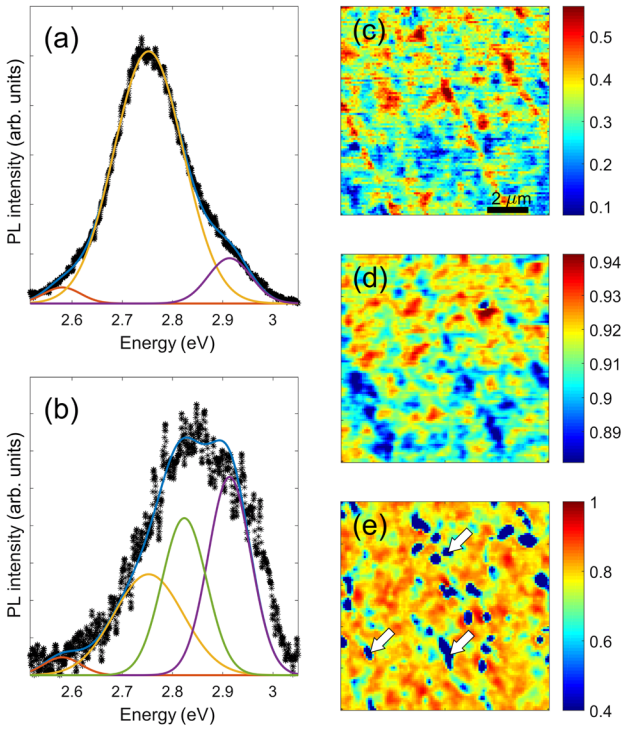

FIG. 7. Near-field PL spectra of the miscut QW for $\mathbf{E}\perp\mathbf{c}$ (a) and $\mathbf{E}\|\mathbf{c}$ (b) polarizations showing deconvolution into Gaussian peaks. Spatial distribution of DLP for high-energy (c), main (d), and low-energy tail (e) peaks. The white arrows in part (e) indicate regions with strain relaxation around defects.

the peak wavelength of the middle peak; (iii) the peak wavelength of short wavelength peak is chosen as the short wavelength shoulder of the $\mathbf{E}\|\mathbf{c}$ spectrum; (iv) an additional peak located 92 meV lower than the second VBL peak is added for $\mathbf{E}\|\mathbf{c}$ to account for a strong phonon replica observed for this polarization [38–40] (see Supplemental Material [34]); (v) the peak wavelength of the long wavelength peak, reflecting the contribution of the deep localized states, is obtained from the best fit. Intensity values of the constituent peaks are allowed to vary as free parameters.

DLP maps for the three PL components for the miscut QW are shown in Figs. 7(c)–7(e). Let us briefly discuss the polarization properties of the different peaks. The DLP of the main peak for both samples has little spatial variation with average values of about 0.92 and standard deviations of 0.02. The division of the PL peak into the three components largely eliminates the contribution of transitions to the second VBL, and the main peak DLP reflects properties of the ground-state transitions.

For the long wavelength peak, the average DLP is smaller (about 0.7), and the standard deviation larger (about 0.2). In some spots, the DLP is below 0.4. Clearly, the symmetry properties of the optical transitions in these areas must differ from those of the ideal bands. Previous standard PL studies related lower DLP in long wavelength tails to confined

exciton states of zero-dimensional symmetry [41] and inclusions of a semipolar phase [22]. Our near-field data suggest that these regions should rather be associated with areas with a partial strain relaxation (presumably, around dislocations), because the low DLP areas are few, and the DLP in these spots is much lower than expected for the semipolar phases [23,42]. Besides, in these regions the peak wavelength is longer, as should be expected for strain-relaxed regions. One should note that the small DLP spots are observed only for the long wavelength component of the PL spectrum, which accounts for just a few percent of the overall PL. There are no analogous low DLP areas in the main peak map. This is yet another indication that the full carrier thermalization does not occur, and that many holes stay in shallower potential minima not related to the deep states of relaxed strain. Hence, the DLP of the cumulative PL remains high throughout the scanned regions.

The DLP of the short wavelength peak is small and experiences large fluctuations ($\sigma = 0.11$). A reduction of the DLP occurs because at these wavelengths PL is a mixture of transitions to the first and second VBLs with opposite polarizations. The large spatial variation can be explained by the different effective band potentials of the VBLs and the spatial variation of the interlevel energy discussed in Sec. III C. A strongly varying interlevel energy would induce a strong variation of the second VBL population and the short wavelength peak DLP.

IV. CONCLUSIONS

A scanning near-field optical microscopy technique has been developed to map the degree of linear PL polarization. The technique has been applied to study polarization properties of wide *m*-plane $In_xGa_{1-x}N/GaN$ QWs grown on on-axis and miscut GaN substrates. The large temperature shift of the PL and DLP spectra, as well as the large DLP values in the near-field scans, show that emission in the QWs takes place from localized states, induced by alloy composition fluctuations. For the on-axis samples, some correlation between the features of the surface morphology and the peak wavelength is observed; however, the morphology-related wavelength variations are small compared to the ones induced by the alloy composition fluctuations. The large PL peak difference for the $\mathbf{E}\|\mathbf{c}$ and $\mathbf{E}\perp\mathbf{c}$ polarizations, the small correlation between the peak wavelength and the DLP, and the DLP temperature dependence suggest that variations of the effective hole potential landscape are much smaller for the second hole level than for the first level. DLP maps for the long wavelength emission revealed regions with a low degree of linear polarization that are attributed to relaxed strain areas around dislocations.

ACKNOWLEDGMENTS

The research at KTH was performed within the frame of Linnaeus Excellence Center for Advanced Optics and Photonics (ADOPT) and was financially supported by the Swedish Energy Agency (Contract No. 36652-1) and the Swedish Research Council (Contract No. 621-2013-4096). The work at UCSB was supported by the Solid State Lighting and Energy Electronics Center (SSLEEC). O. Martnez acknowledges the financial support from the Ayudas del Plan de Movilidad de Investigadores program of the University of Valladolid.

[1] T. Y. Lin, P. K. Wei, E. H. Lin, T. L. Tseng, and R. Chang, Investigation on the correlation between the crystalline and optical properties of InGaN using near-field scanning optical microscopy, Electrochem. Solid State Lett. **10**, H217 (2007).

[2] A. Pinos, V. Liuolia, S. Marcinkevičius, J. Yang, R. Gaska, and M. S. Shur, Localization potentials in AlGaN epitaxial films studied by scanning near-field optical spectroscopy, J. Appl. Phys. **109**, 113516 (2011).

[3] M. S. Jeong, J. Y. Kim, Y.-W. Kim, J. O. White, E.-K. Suh, C.-H. Hong, and H. J. Lee, Spatially resolved photoluminescence in InGaN/GaN quantum wells by near-field scanning optical microscopy, Appl. Phys. Lett. **79**, 976 (2001).

[4] F. Hitzel, G. Klewer, S. Lahmann, U. Rossow, and A. Hangleiter, Localized high-energy emissions from the vicinity of defects in high-efficiency $Ga_xIn_{1-x}N/GaN$ quantum wells, Phys. Rev. B **72**, 081309 (2005).

[5] K. Okamoto, A. Scherer, and Y. Kawakami, Near-field scanning optical microscopic transient lens for carrier dynamics study in InGaN/GaN quantum wells, Appl. Phys. Lett. **87**, 161104 (2005).

[6] A. Kaneta, M. Funato, and Y. Kawakami, Nanoscopic recombination processes in InGaN/GaN quantum wells emitting violet, blue, and green spectra, Phys. Rev. B **78**, 125317 (2008).

[7] A. Kaneta, Y.-S. Kim, M. Funato, Y. Kawakami, Y. Enya, T. Kyono, M. Ueno, and T. Nakamura, Nanoscopic photoluminescence properties of a green-emitting InGaN single quantum well on a $(20\bar{2}1)$ GaN substrate probed by scanning near-field optical microscopy, Appl. Phys. Express **5**, 102104 (2012).

[8] S. Marcinkevičius, K. M. Kelchner, S. Nakamura, S. P. DenBaars, and J. S. Speck, Optical properties of extended and localized states in *m*-plane InGaN quantum wells, Appl. Phys. Lett. **102**, 101102 (2013).

[9] S. Marcinkevičius, Y. Zhao, K. M. Kelchner, S. Nakamura, S. P. DenBaars, and J. S. Speck, Near-field investigation of spatial variations of $(20\bar{2}\,\bar{1})$ InGaN quantum well emission spectra, Appl. Phys. Lett. **103**, 131116 (2013).

[10] K. Gelžinytė, R. Ivanov, S. Marcinkevičius, Y. Zhao, D. L. Becerra, S. Nakamura, S. P. DenBaars, and J. S. Speck, High spatial uniformity of photoluminescence spectra in semipolar $(20\bar{2}1)$ plane InGaN/GaN quantum wells, J. Appl. Phys. **117**, 023111 (2015).

[11] A. Vertikov, A. V. Nurmikko, K. Doverspike, G. Bulman, and J. Edmond, Role of localized and extended electronic states in InGaN/GaN quantum wells under high injection,

inferred from near-field optical microscopy, Appl. Phys. Lett. **73**, 493 (1998).

[12] S. Marcinkevičius, K. Gelžinytė, Y Zhao, S. Nakamura, S. P. DenBaars, and J. S. Speck, Carrier redistribution between different potential sites in semipolar $(20\bar{2}1)$ InGaN quantum wells studied by near-field photoluminescence, Appl. Phys. Lett. **105**, 111108 (2014).

[13] A. Kaneta, T. Hashimoto, K. Nishimura, M. Funato, and Y. Kawakami, Visualization of the local carrier dynamics in an InGaN quantum well using dual-probe scanning near-field optical microscopy, Appl. Phys. Express **3**, 102102 (2010).

[14] N. Rotenberg and L. Kuipers, Mapping nanoscale light fields, Nat. Photonics **8**, 919 (2014).

[15] R. Micheletto, M. Allegrini, and Y. Kawakami, Near-field evidence of local polarized emission centers in InGaN/GaN materials, Appl. Phys. Lett. **95**, 211904 (2009).

[16] S. Ghosh, P. Waltereit, O. Brandt, H. T. Grahn, and K. H. Ploog, Electronic band structure of wurtzite GaN under biaxial strain in the *m*-plane investigated with photoreflectance spectroscopy, Phys. Rev. B **65**, 075202 (2002).

[17] L. Schade, U. T. Schwarz, T. Wernicke, M. Weyers, and M. Kneissl, Impact of band structure and transition matrix elements on polarization properties of the photoluminescence of semipolar and nonpolar InGaN quantum wells, Phys. Status Solidi (b) **248**, 638 (2011).

[18] H. Masui, H. Yamada, K. Iso, J. S. Speck, S. Nakamura, and S. P. DenBaars, Nonpolar-oriented InGaN light-emitting diodes for liquid-crystal-display backlighting, J. Soc. Inf. Disp. **16**, 571 (2008).

[19] S. Sakai and A. A. Yamaguchi, Theoretical analysis of optical polarization properties in semipolar and nonpolar InGaN quantum wells for precise determination of valence-band parameters in InGaN alloy material, Phys. Status Solidi (b) **252**, 885 (2015).

[20] T. Onuma, T. Koyama, A. Chakraborty, M. McLaurin, B. A. Haskell, P. T. Fini, S. Keller, S. P. DenBaars, J. S. Speck, S. Nakamura, U. K. Mishra, T. Sota, and S. F. Chichibu, Radiative and nonradiative lifetimes in nonpolar *m*-plane InGaN/GaN multiple quantum wells grown on GaN templates prepared by lateral epitaxial overgrowth, J. Vac. Sci. Technol. B **25**, 1524 (2007).

[21] V. Liuolia, S. Marcinkevičius, Y.-D. Lin, H. Ohta, S. P. DenBaars, and S. Nakamura, Dynamics of polarized photoluminescence in *m*-plane InGaN/GaN quantum wells, J. Appl. Phys. **108**, 023101 (2010).

[22] S. Schulz, D. P. Tanner, E. P. O'Reilly, M. A. Caro, T. L. Martin, P. A. J. Bagot, M. P. Moody, F. Tang, J. T. Griffiths, F. Oehler, M. J. Kappers, R. A. Oliver, C. J. Humphreys, D. Sutherland, M. J. Davies, and P. Dawson, Structural, electronic, and optical properties of *m*-plane InGaN/GaN quantum wells: Insights from experiment and atomistic theory, Phys. Rev. B **92**, 235419 (2015).

[23] C. Mounir, U. T. Schwarz, I. L. Koslow, M. Kneissl, T. Wernicke, T. Schimpke, and M. Strassburg, Impact of inhomogeneous broadening on optical polarization of high-inclination semipolar and nonpolar $In_xGa_{1-x}N$/GaN quantum wells, Phys. Rev. B **93**, 235314 (2016).

[24] K. M. Kelchner, L. Y. Kuritzky, Kenji Fujito, S. Nakamura, S. P. DenBaars, and J. S. Speck, Emission characteristics of single InGaN quantum wells on misoriented nonpolar *m*-plane bulk GaN substrates, J. Cryst. Growth **382**, 80 (2013).

[25] W. Shan, T. J. Schmidt, X. H. Yang, S. J. Hwang, J. J. Song, and B. Goldenberg, Temperature dependence of interband transitions in GaN grown by metalorganic chemical vapor deposition, Appl. Phys. Lett. **66**, 985 (1995).

[26] P. Dawson, S. Schulz, R. A. Oliver, M. J. Kappers, and C. J. Humphreys, The nature of carrier localisation in polar and nonpolar InGaN/GaN quantum wells, J. Appl. Phys. **119**, 181505 (2016).

[27] M. Kubota, K. Okamoto, T. Tanaka, and H. Ohta, Temperature dependence of polarized photoluminescence from nonpolar *m*-plane InGaN multiple quantum wells for blue laser diodes, Appl. Phys. Lett. **92**, 011920 (2008).

[28] K. M. Kelchner, L. Y. Kuritzky, S. Nakamura, S. P. DenBaars, and J. S. Speck, Stable vicinal step orientations in *m*-plane GaN, J. Cryst. Growth **411**, 56 (2015).

[29] V. Liuolia, A. Pinos, S. Marcinkevičius, Y.-D. Lin, H. Ohta, S. P. DenBaars, and S. Nakamura, Carrier localization in *m*-plane InGaN/GaN quantum wells probed by scanning near-field optical spectroscopy, Appl. Phys. Lett. **97**, 151106 (2010).

[30] D. Watson-Parris, M. J. Godfrey, P. Dawson, R. A. Oliver, M. J. Galtrey, M. J. Kappers, and C. J. Humphreys, Carrier localization mechanisms in $In_xGa_{1-x}N$/GaN quantum wells, Phys. Rev. B **83**, 115321 (2011).

[31] T.-J. Yang, R. Shivaraman, J. S. Speck, and Y.-R. Wu, The influence of random indium alloy fluctuations in indium gallium nitride quantum wells on the device behavior, J. Appl. Phys. **116**, 113104 (2014).

[32] T. Hanada, *Oxide and Nitride Semiconductors: Processing, Properties, and Applications*, edited by T. Yao and S.-K. Hong (Springer Science & Business Media, Berlin, 2009).

[33] S.-H. Park, D. Ahn, and S.-L. Chuang, Electronic and optical properties of *a*- and *m*-plane wurtzite InGaN/GaN quantum wells, IEEE J. Quant. Electron. **43**, 1175 (2007).

[34] See Supplemental Material at http://link.aps.org/supplemental/10.1103/PhysRevApplied.7.064033 for the detailed derivation of Eq. (2) and the manifestation of the phonon replica in PL spectra.

[35] S. L. Chuang and C. S. Chang, A band-structure model of strained quantum-well wurtzite semiconductors, Semicond. Sci. Technol. **12**, 252 (1997).

[36] K. Kojima, H. Kamon, M. Funato, and Y. Kawakami, Theoretical investigations on anisotropic optical properties in semipolar and nonpolar InGaN quantum wells, Phys. Status Solidi (c) **5**, 3038 (2008).

[37] P. G. Eliseev, P. Perlin, J. Lee, and M. Osiński, Blue temperature-induced shift and band-tail emission in InGaN-based light sources, Appl. Phys. Lett. **71**, 569 (1997).

[38] X. B. Zhang, T. Taliercio, S. Kolliakos, and P. Lefebvre, Influence of electron-phonon interaction on the optical properties of III-nitride semiconductors, J. Phys. Condens. Matter **13**, 7053 (2001).

[39] D. Chen, Y. Luo, L. Wang, H. Li, G. Xi, Y. Jiang, Z. Hao, C. Sun, and Y. Han, Enhancement of electron-longitudinal optical phonon coupling in highly strained InGaN/GaN quantum well structures, J. Appl. Phys. **101**, 053712 (2007).

[40] S. Kalliakos, X. B. Zhang, T. Taliercio, P. Lefebvre, B. Gil, N. Grandjean, B. Damilano, and J. Massies, Large size dependence of exciton-longitudinal-optical-phonon coupling in nitride-based quantum wells and quantum boxes, Appl. Phys. Lett. **80**, 428 (2002).

[41] Y. J. Sun, O. Brandt, M. Ramsteiner, H. T. Grahn, and K. H. Ploog, Polarization anisotropy of the photoluminescence of *m*-plane $(\mathrm{In,Ga})\mathrm{N}/\mathrm{GaN}$ multiple quantum wells, Appl. Phys. Lett. **82**, 3850 (2003).

[42] S. Marcinkevičius, R. Ivanov, Y. Zhao, S. Nakamura, S. P. DenBaars, and J. S. Speck, Highly polarized photoluminescence and its dynamics in semipolar $(20\bar{2}\,\bar{1})$ $\mathrm{InGaN}/\mathrm{GaN}$ quantum well, Appl. Phys. Lett. **104**, 111113 (2014).